Journal of Materials Chemistry A

ROYAL SOCIETY OF CHEMISTRY

PAPER

View Article Online
View Journal | View Issue

Cite this: J. Mater. Chem. A, 2021, 9, 16086

A universal strategy towards 3D printable nanomaterial inks for superior cellular high-loading battery electrodes†

Xiaocong Tian,[ab] Teng Wang,[ac] Hui Ma,[a] Kang Tang,[ab] Shuen Hou,[a] Hongyun Jin *[a] and Guozhong Cao [d]

Direct ink writing has emerged as one of the simplest 3D printing technologies for a wide range of applications including energy storage devices. Inks with high printability and desired functionality are the most important elements to achieve efficient 3D printing. Many printable inks have been reported; however, few were developed with high versality. In this paper, a versatile fabrication approach for various desirable 3D printable nanomaterial inks is presented for superior battery electrodes. By controlling the dispersing solvents, the inks' rheological properties are well tailored for 3D printing processes without sacrificing the weight ratio of electrode components. At high mass loading, 3D printed cellular $LiFePO_4$ cathodes and $Li_4Ti_5O_{12}$ anodes deliver high specific capacities of 168 (0.5C) and 171 mA h g^{-1} (1C), respectively, which are both close to their corresponding theoretical capacities. Meanwhile, high-rate capabilities and superior long-term cycling stabilities are also demonstrated for the obtained cellular high-loading cathodes and anodes. A 3D printed Li-ion full-cell battery also exhibits outstanding electrochemical performance. This work presents a strategy with high versality for advanced 3D printable nanomaterial inks for next-generation customized and high-performance energy storage devices.

Received 17th April 2021
Accepted 18th June 2021

DOI: 10.1039/d1ta03236d

rsc.li/materials-a

Introduction

With the growing consumption of energy and increasing demand for sustainable energy systems, the energy storage technology is playing a more and more critical role in modern lives.[1–5] Due to their high energy density, moderate power density, no memory effect and long life span, advanced rechargeable batteries have attracted extensive attention in industrial fields ranging from portable electronics to electric vehicles (EVs).[6,7] Lithium batteries are one of the best rechargeable battery technologies and have thus witnessed significant success for various commercial applications. To achieve satisfactory electrochemical performances and lowering of costs of lithium-ion batteries, the electrode configuration as well as the corresponding manufacturing technique is of great importance.[8–12] To date, although various manufacturing techniques have been reported, direct customized configuration design with advanced battery electrode production capability has been regarded as a significant challenge and is thus expected to be achieved for future applications.[13–16]

3D printing has recently been recognized as an emerging manufacturing technique to fabricate considerable battery and supercapacitor electrodes with customized configuration designs, structural optimization, rapid prototyping and promising electrochemical performance.[17–21] To date, various 3D printing approaches have been employed to design and fabricate functional materials, among which direct ink writing (DIW) is a cost-efficient and versatile one with a strong capability to directly achieve the 3D construction *via* the facile ink extrusion.[22–26] Hu *et al.* used DIW to obtain a 3D printed $LiMn_{1-x}Fe_xPO_4$ nanocrystal cathode which delivered a much better electrochemical performance than the traditional battery electrode.[27] Yao *et al.* constructed a porous carbon aerogel scaffold *via* a DIW strategy to realize the ultrahigh loading of the pseudocapacitive component for supercapacitor applications.[28] These pioneering research studies indicate that the DIW approach is a powerful platform for fabricating electrochemical energy storage electrodes.

Using the powerful DIW printing technique, the delivered electrochemical performance can be well tuned *via* the control of composition and microstructure of the printed materials.[29–32] Among the various constructed 3D structures, cellular materials are regarded as a unique but one of the most representative

[a]Faculty of Materials Science and Chemistry, China University of Geosciences, Wuhan 430074, China. E-mail: jinhongyun@cug.edu.cn
[b]Zhejiang Institute, China University of Geosciences, Hangzhou, 311305, China
[c]The Institute of Technological Sciences, Wuhan University, Wuhan, 430072, China
[d]Department of Materials Science & Engineering, University of Washington, WA 98195, USA

† Electronic supplementary information (ESI) available. See DOI: 10.1039/d1ta03236d

configurations inspired by nature and possess great advantages for diverse application fields especially for advanced electrochemical energy storage.[33–35] Previous studies have demonstrated that the inherent ink preparation is core for the printing process and printed electrodes. On the one hand, to achieve continuous ink extrusion as well as ink solid-like stacking, the difficulty lies in tuning of the ink's rheological properties.[36] On the other hand, the ink formulation directly affects the electrochemical performance of printed electrodes. To date, although some pioneering work has been reported to obtain printable inks for electrochemical energy storage applications, the key to access 3D printable nanomaterial inks was not reported and a universal route with high controllability in electrode formulation is still lacking, which largely hinders the further utilization of 3D printed electrochemical energy storage devices or components.[37,38]

Here, we report a universal approach towards various desirable 3D printable nanomaterial inks for superior cellular battery electrodes with high mass loading. The volume (dispersing solvent) to solid mass (including active material, conducting agent and binder) ratio (VMT) is found to be a general element to access the printability of ink. By tuning VMT in a specific range, all obtained inks with different compositions deliver the desired rheological properties without sacrificing the controllability of each electrode component. To demonstrate the universality of our route, commercial $LiFePO_4$ (LFP) and $Li_4Ti_5O_{12}$ (LTO) powders are utilized directly and set as typical examples in this work, while carbon nanotubes (CNTs) and reduced graphene oxide (rGO) are employed as conductive agents. All prepared inks show desired viscosities and stable solid-like fluid properties, resulting in successful extrusion processes. 3D printed cellular battery cathodes and anodes possess high mass-loading characteristics and exhibit superior specific capacities (close to the theoretical capacities), rate capabilities and cycling stabilities at the same time. When a 3D printed cathode and anode are assembled into a full-cell, excellent electrochemical performance is still observed, which is due to the continuous 3D electron transport, large electrode–electrolyte contact and shortened ion diffusion distance. This universal ink preparation route offers great advantages in battery additive manufacturing and holds tremendous promise in leading the battery into a new application realm.

Results and discussion

Fig. 1a–c illustrate the typical fabrication process of various Li-ion battery electrodes by DIW-based 3D printing. Generally, moderate viscosity, good fluidity and high controllability are desired characteristics for printable inks. In this work, such inks were simply prepared with a mortar by the full grinding of active materials, conductive agents, and binder in a weight ratio of 7 : 2 : 1 (Fig. 1d). It is found that the key to achieve 3D printable rheological properties without changing the solid components of inks is the control of dispersing solvent content. Using the obtained printable electrode inks, cellular electrodes were extruded on a glass substrate (Fig. 1e and f) at a constant speed through a 330 μm nozzle. The designed cellular structure

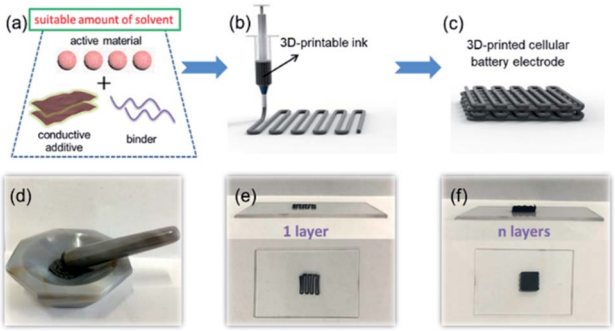

Fig. 1 (a–c) Schematic of the DIW-based 3D printing process of cellular battery electrodes. (d–f) Optical images of (d) printable ink, and (e) 1-layer-printed and (f) *n*-layer-printed cellular battery electrode architectures.

contains open-periodic pores, which indicates the further enhanced kinetics of electron and ion transport during the charge–discharge process.[39] The nominal area of the printed battery electrodes was approximately 0.49 cm^2, while the actual area was 0.28 cm^2.

To reveal a key element to access the printable electrode inks, different contents (1 mL, 3 mL and 5 mL) of *N*-methyl-2-pyrrolidone (NMP) solvents were added to disperse the same electrode solids (for example, the LFP–rGO cathode which includes an active material, conductive agent, and binder) with a total amount of 1 g. As shown in Fig. 2a and b, the flowing states of obtained inks with different solvents were significantly different. The addition of 1 mL solvent did not enable the mixture to become a homogeneous ink and obvious agglomeration was observed, implying that a smooth extrusion was improbable in the following step. As the dispersing solvent amount increases to 3 mL and 5 mL, homogeneous inks were formed, while an obvious backflow phenomenon was found for the 5 mL solvent-contained bottle when it was placed upside

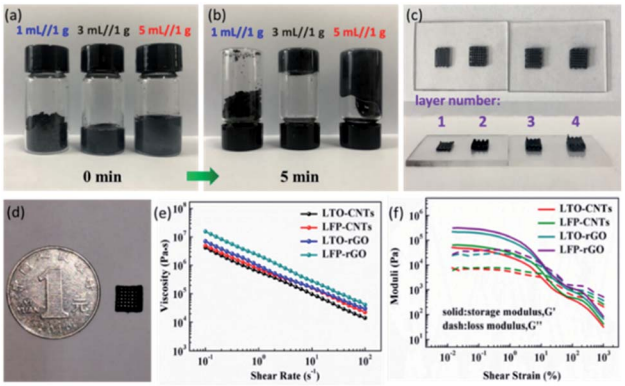

Fig. 2 (a and b) Photographs of nanomaterial inks with different solvent contents in bottles placed (a) upright and (b) upside down after 5 min. (c) Photograph of 3D printed cellular battery electrodes with different printing layers. (d) Comparison between a 4-layer-printed battery electrode and a coin. (e) Viscosity–shear rate relationship and (f) modulus–shear strain relationship of various 3D printable nanomaterial inks.

down for 5 min. Such backflowing indicates the low viscosity and ease of levelling after the extrusion. It worth noting that the ink with 3 mL of solvent showed a high viscosity state without backflowing. Using the 3 mL/1 g one, different layers of battery electrodes were printed through the DIW technique as shown in Fig. 2c and the area of the as-printed electrode was less than half the area of a coin (Fig. 2d).

In order to quantitatively understand the importance of VMT in electrode inks, the rheological properties of four different kinds of inks (LFP–rGO, LFP–CNTs, LTO–rGO, and LTO–CNTs) were studied. Fig. 2e displays the apparent viscosity–shear rate relationship of these inks measured at room temperature for 10 minutes. The apparent viscosities of the four types of ink decreased with the increase of shear rates, which illustrated their shear thinning properties and showed that the prepared inks were non-Newtonian fluids. When the shear rate was 0.1 s^{-1}, the maximum apparent viscosities of both LFP-based and LTO-based battery inks exceeded or almost reached 10^7 Pa s, which was beneficial for the DIW-based printing process. It also revealed that inks prepared through our VMT tuning has excellent controllability and universality in delivered rheological properties. Fig. 2f presents the modulus values of battery electrode inks changing with shear strain, showing that the storage moduli of both LFP-based and LTO-based battery inks were higher than the loss moduli and they kept almost unchanged when the shear strain was low. With the continuous increase of shear strain, the loss moduli exceeded the corresponding storage moduli, reflecting a solid-like behavior for all obtained inks. The above results fully demonstrated that, with the precise control of VMTs in electrode inks, 3D printable rheological properties were available for various ink formulations. This was a good illustration that our proposed approach was a universal route for 3D printed battery electrode applications.

After clarifying the 3D printable rheological properties of inks, X-ray diffractometer (XRD) and scanning electron microscopy (SEM) studies were performed to uncover the structural information of the as-printed battery electrodes as shown in Fig. S1 and S3.† All characteristic peaks observed in the XRD patterns of both LFP-based and LTO-based battery electrodes can be completely indexed to pure LFP and LTO phases (Fig. S1†), respectively, illustrating that chemical

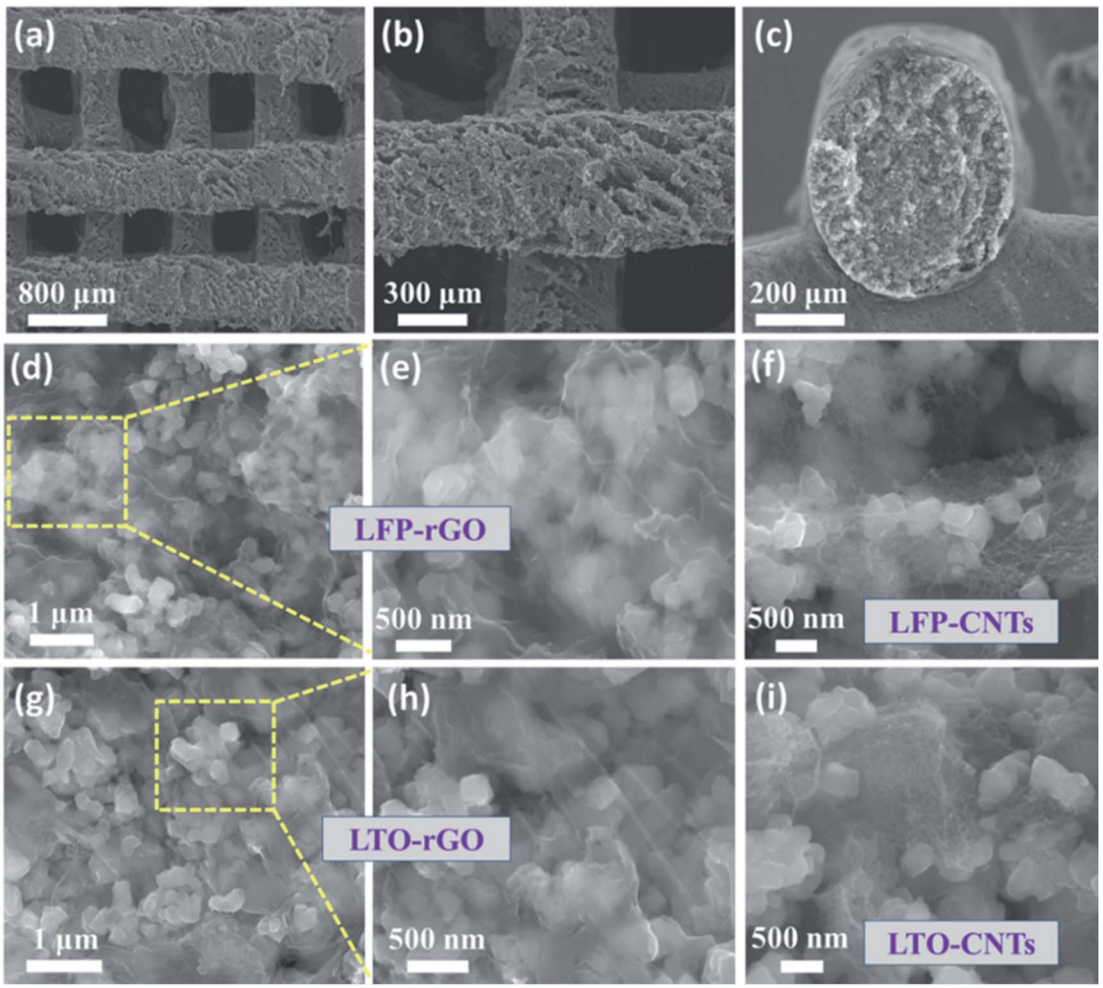

Fig. 3 (a–c) Low-magnification SEM images of the as-printed cellular battery electrodes. (d–f) SEM images of (d and e) LFP–rGO and (f) LFP–CNT electrodes at high magnification. (g–i) SEM images of (g and h) LTO–rGO and (i) LTO–CNT electrodes at high magnification.

components were not destroyed during the 3D printing processes. As seen from low-magnification SEM images, the 3D printed battery electrode presented a periodic cellular structure connected with horizontal and vertical printing lines (Fig. 3a and b). Additionally, cylindrical shapes of each line were observed as shown in Fig. 3c and all diameters of these lines were approximately 350 μm, which were consistent with the nozzle inner diameter, further implying the solid-like extrusion properties and desired controllability of inks. It was acknowledged that the cellular structure with open macropores was favourable for the initial infiltration and penetration of electrolyte ions during the charge–discharge processes, thus offering more accessible sites and further leading to improved electrochemical performance.

At high magnifications, the morphologies and microstructures of the as-printed LFP-based and LTO-based battery electrodes were studied as shown in Fig. 3d–i. It was clearly seen that nanostructured LFP particles (~300 nm in diameter) were finely dispersed and embedded with rGO nanosheets. In the resultant 3D LFP–rGO framework, irregular macroscopic and microscopic pores formed as shown in Fig. 3d and e, which may be due to the freeze-drying treatment during the electrode fabrication. For LFP–CNT battery electrodes, a similar good dispersity phenomenon was found (Fig. 3f), where LFP nanoparticles well bundled with CNTs, implying the desired electrical transport for the whole printed structure. It is worth noting that the above structural results were also applicable for the as-printed LTO–rGO and LTO–CNT battery electrodes as shown in Fig. 3g–i, illustrating the high versatility and promise of our approach.

To evaluate the electrochemical performance of various 3D printed battery electrodes, we first assembled LFP-based and LTO-based Li-ion coin-type half-cells, for which rGO and CNTs were added as two forms of conductive agent, respectively. At a rate of 0.5C, the 3-layer-printed LFP–rGO cathode with a 16.3 mg cm^{-2} mass loading (calculated from the actual area) delivered discharge capacities up to 168 mA h g^{-1}, which was very close to its theoretical capacity of ~170 mA h g^{-1}. The characteristic voltage plateau upon lithiation and delithiation was also observed with the cathodic and anodic peaks in cyclic voltammetry (CV) curves (Fig. S2 and S3†). As the rate increased to 1C, 1.5C, 2C and 3C, its discharge capacities still remained at 151, 138, 134 and 125 mA h g^{-1}, respectively (Fig. 4a). Importantly, the discharge capacities at high rates were achieved under high mass loading conditions, implying a reasonable cellular structural design during the fast ion transport for 3D printed LFP–rGO cathodes. In the presence of nanostructured carbon agents, both forms of LFP-based cathodes showed small voltage polarization as depicted in Fig. 4b, while the rGO-added one showed a higher capacity which may be due to the formation of a homogeneous conductive carbon network.

The rate performance of the as-printed LFP–rGO cathodes was further measured at various rates ranging from 0.5C to 3C (Fig. 4c). Among the various cathodes, the 1-layer-printed one possessed the highest reversible discharge capacities at various rates, indicating ultrafast lithium storage. When the rate returned to 0.5C, exceeded specific capacities were obtained for most cathodes even with 4-printing-layers, implying ultrafast lithium storage performance. With digital control of the electrode printing layer and thickness, the areal mass loading of LFP printed from 1 to 4 layers was 6.2, 11.5, 16.3 and 25.6 mg cm^{-2}, respectively. Accordingly, the specific areal capacities enlarged linearly as displayed in Fig. 4d, indicating an advantageous electrochemical behavior of thick electrodes compared

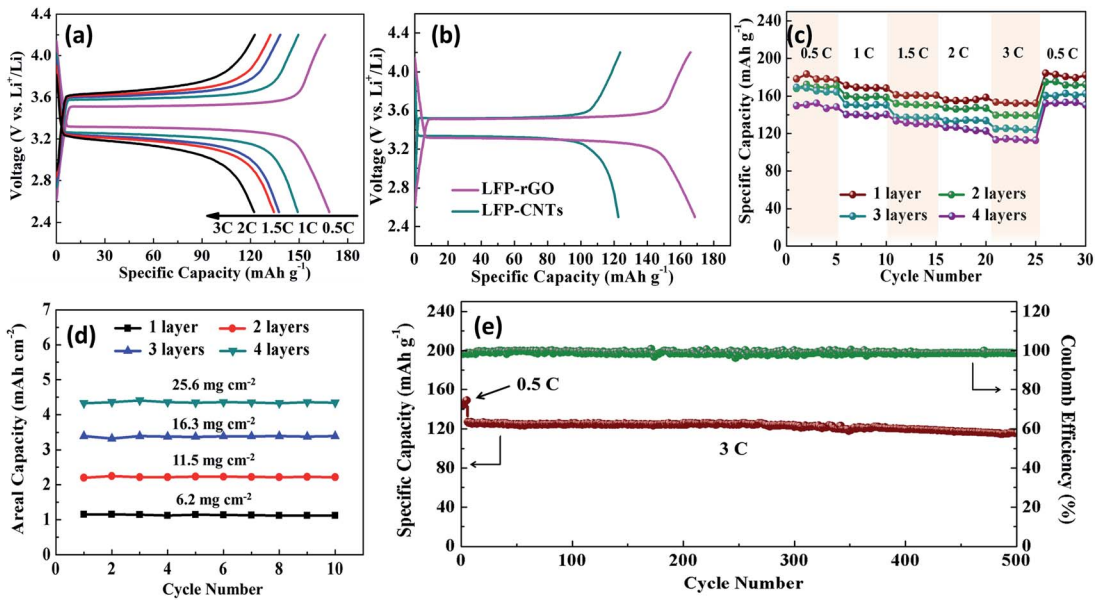

Fig. 4 Electrochemical performance of Li-ion half-cells assembled with 3D-printed LFP-based cathodes. (a and b) GCD profiles of 3-layer-printed LFP–rGO electrodes at different rates (a) and LFP–rGO and LFP–CNT electrodes at 0.5C (b). (c and d) Rate capability obtained from 0.5C to 3C (c) and areal capacity evolution profiles (d) of LFP–rGO electrodes with different printing layers. (e) Long-term cycling performance of 3-layer-printed LFP–rGO electrodes over 500 cycles at a rate of 3C.

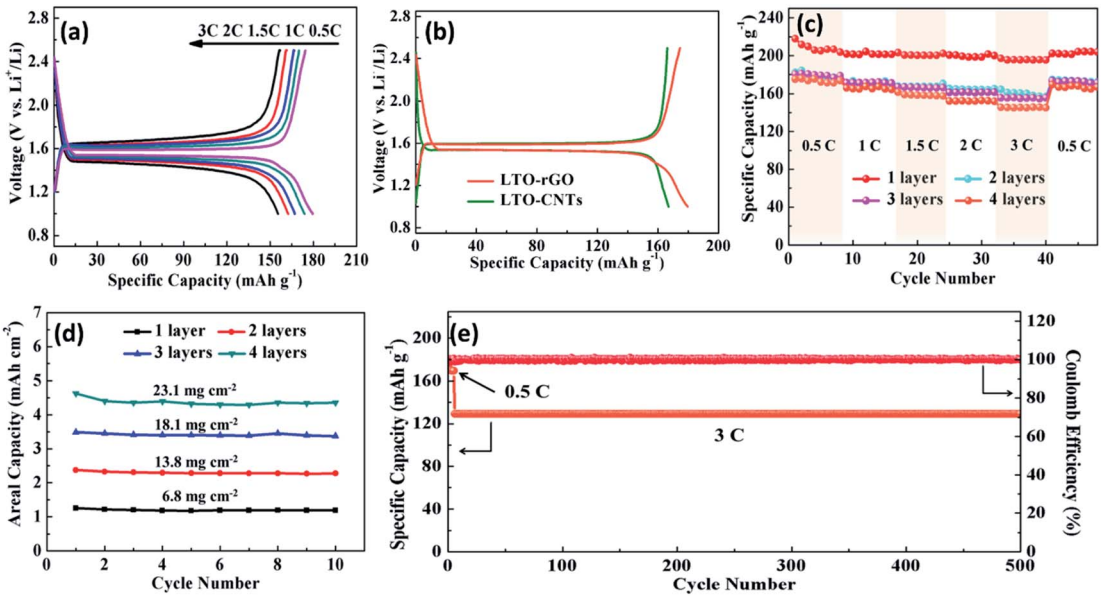

Fig. 5 Electrochemical performance of Li-ion half-cells assembled with 3D-printed LTO-based anodes. GCD profiles of (a) 3-layer-printed LTO–rGO anodes at different rates and (b) LTO–rGO and LTO–CNT anodes at 0.5C. (c) Rate capability obtained from 0.5C to 3C and (d) areal capacity evolution profiles of LTO–rGO electrodes with different printing layers. (e) Long-term cycling performance of 3-layer-printed LTO–rGO electrodes over 500 cycles at a rate of 3C.

with conventionally manufactured ones. After almost 500 long-term charge and discharge cycles at 3C, 116 mA h g^{-1} was still obtained as shown in Fig. 4e, corresponding to an ultrahigh capacity retention of 99% for thick 3-layer-printed cathodes.

The electrochemical performance of LTO-based anodes is shown in Fig. 5. At a rate of 0.5C, the specific discharge capacity of the 3-layer-printed LTO–rGO anode with high mass loading was 180 mA h g^{-1} (Fig. 5a), even exceeding its theoretical capacity of ~175 mA h g^{-1}, which may be due to the introduction of rGO components.[40,41] Ultrasmall voltage polarization values were found for rGO-added and CNT-added anodes (Fig. 5b). Similar to LFP-based cathodes, the characteristic voltage plateau upon lithiation and delithiation was also observed with cathodic and anodic peaks in CV curves (Fig. S4 and S5†). Remarkably, excellent rate capabilities were observed for all LTO–rGO anodes with different printing layers (Fig. 5c). Even 1-layer-printed anodes did not show a noticeable capacity decline when rates increased from 0.5C to 3C. At rates of 1, 1.5, 2 and 3C, the specific capacities of 3-layer-printed anodes still remained at 171, 166, 162 and 155 mA h g^{-1}, respectively. As depicted in Fig. 5d, the linearly enlarged areal capacities further demonstrated the 3D printed cellular design which was beneficial for the electron and ion transport during lithiation and delithiation processes. The long-term cycling stability of the LTO–rGO anodes is displayed in Fig. 5e, which shows that an outstanding capacity retention of 99.9% was achieved for almost 500 charge and discharge cycles.

Compared with conventional manufacturing electrodes, the microstructure of the 3D printed electrodes can be well tuned. Our cellular electrodes present a typical form which offers huge advantages including 3D electron transport, large electrode–electrolyte contact and shortened ion diffusion distance as schematically shown in Fig. 6a. These features enabled desired electron and ion transport even for thick electrodes. Our universal route is the key to access printable inks, and thus provides an excellent platform for future practical applications

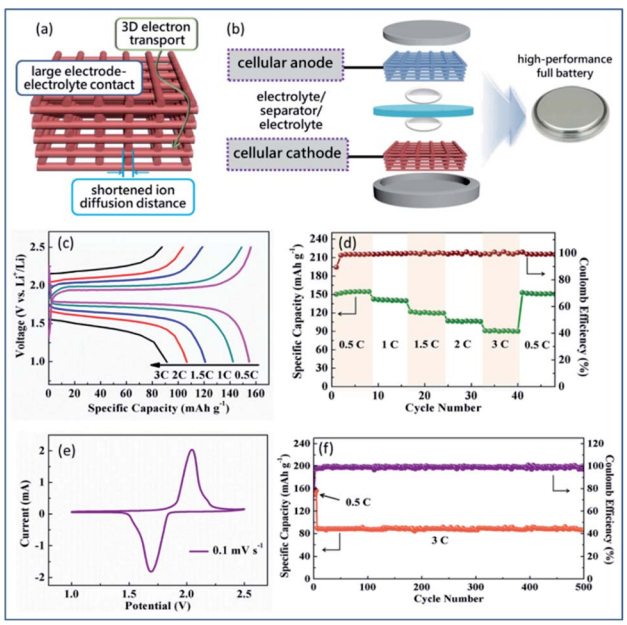

Fig. 6 Schematics and electrochemical performance of all-3D-printed Li-ion full-cells. (a and b) Schematics of benefits of 3D-printed electrodes (a) and the assembled all-3D-printed Li-ion coin-type full-cell structure (b). (c and d) The GCD profiles (c) and rate performance (d) of all-3D-printed Li-ion full-cells at different rates. (e) The CV curve of all-3D-printed Li-ion full-cells at 0.1 mV s^{-1}. (f) Long-term cycling performance of all-3D-printed Li-ion full-cells.

of 3D printed electrodes. Our 3D printed electrode architectures are also applicable to other energy storage systems such as Li–S batteries, Li–Se batteries, and Li–O_2 batteries.[33]

A coin-type full-cell was assembled with a 3D printed LFP–rGO cathode and LTO–rGO anode, both of which had 2 printing layers (Fig. 6b). Remarkably, this all-3D printed full-cell still exhibited a characteristic voltage plateau and superior discharge capacities at various rates as shown in Fig. 6c, confirming the outstanding applicability of our 3D printed thick electrode structures. The rate performance was further measured at various rates ranging from 0.5C to 3C (Fig. 6d). Highly reversible capacities of 155, 140, 119, 107 and 91 mA h g^{-1} were achieved at 0.5, 1, 1.5, 2 and 3C, respectively. When the rate returned to 0.5C, a remarkable capacity of 151.8 mA h g^{-1} and a corresponding high retention of 98.3% were obtained. The phenomenon of lithiation and delithiation was also observed in the CV curve of all-3D-printed Li-ion full-cells at 0.1 mV s^{-1} (Fig. 6e). During long-term cycling processes, the full-cell delivered an outstanding capacity retention of 98% for almost 500 cycles (Fig. 6f). The electrochemical performance clearly illustrated the great advancement in 3D printing for electrochemical energy storage, in which printable inks are the most important element towards wide and practical applications.

Conclusions

In conclusion, a simple and universal ink fabrication strategy is proposed by precisely controlling the dispersing solvent amounts in a specific range. Using this general strategy, the rheological properties of the various obtained nanomaterial electrode inks can be well tailored for printing processes. Meanwhile, the high controllability of each ink component is still maintained, providing excellent optimization space for the delivered electrochemical performance. Moreover, this printable ink fabrication enables an ideal platform for designing favourable electrode configurations. At high mass loading, 3D printed cellular $LiFePO_4$ cathodes and $Li_4Ti_5O_{12}$ anodes deliver high specific capacities of 168 (0.5C) and 171 mA h g^{-1} (1C), respectively, which are both close to their corresponding theoretical capacities. Their rate capabilities and cycling stabilities are also remarkable. Moreover, an all-3D-printed full Li-ion battery still exhibits outstanding electrochemical performance, illustrating the great potential of our ink fabrication strategy for future practical energy storage applications.

Experimental

Preparation of 3D printable electrode inks

The electrode solid (active material, conductive agent, and binder with a mass ratio of 7 : 2 : 1) was firstly put into a mortar for grinding for 5 minutes. Then, NMP solvent was added with grinding for 10 minutes and further mixing using a speed mixer (SpeedMixer DAC 150.1). The solvent (volume, in mL) to electrode material (mass, in g) ratios (SER) were tuned to 1 : 1, 3 : 1 and 5 : 1, respectively, to obtain various inks with different solid concentrations. In this work, two kinds of active material, LFP and LTO, were employed, while CNTs and rGO acted as the conductive agents and polyvinylidene fluoride (PVDF) acted as the binder. Thus, four typical 3D printed electrode inks, namely LFP–rGO, LFP–CNTs, LTO–rGO, and LTO–CNTs, were finally obtained.

3D printing of cellular electrodes and battery assembly

Electrode inks were loaded into syringes with a 5 mL volume and nozzles with a diameter of 330 μm. With a constant pressure of 0.1–0.2 MPa driven by pneumatic force, the ink is extruded onto a glass substrate at a constant speed using a 3-axes extrusion system. The configuration and thickness of the printed electrodes were controlled according to computer-aided routines. Finally, the printed electrode materials were immersed in deionized water for 12 h, and then immediately freeze-dried for 5 h.

For the Li-ion half-cell battery, the cells (CR2032) were assembled with the 3D printed cellular electrodes, Li metal anode, separator, and electrolyte (1 M $LiPF_6$). For the Li-ion full-cell battery, the same-type coin-type cells were assembled with a 3D printed cellular LFP-based or LTO-based electrode with different printing layers, separator, and electrolyte (1 M $LiPF_6$). The half-cell and full-cell were assembled in an Ar-filled glovebox.

Structural characterization and electrochemical measurements

The rheological properties of the electrode inks were determined using an Anton Paar 302 rheometer with a flat rotor (25 mm diameter). SEM images were collected on a JEOL-7100F field-emission scanning electron microscope. The crystal structure of the samples was characterized using a powder XRD between 10° and 70° with a scan rate of 5° min^{-1}.

The electrochemical performance of the LFP-based and LTO-based coin-type Li-ion half-cells was measured from 2.5 to 4.3 V and 1.0 to 2.5 V, respectively, at different current densities using a battery testing system (LAND CF-2001A). For electrochemical measurement of the coin-type Li-ion full-cell, the galvanostatic charge–discharge (GCD) window of 1.0 to 2.5 V was used at different rates. Corresponding cyclic voltammetry (CV) data were recorded using a CHI 760D electrochemical workstation. Electrochemical impedance spectroscopy (EIS) was performed from 10^{-2} to 10^5 Hz. All measurements were performed at room temperature.

Author contributions

Xiaocong Tian: conceptualization, data curation, formal analysis, funding acquisition, investigation, methodology, project administration, resources, supervision, validation, writing – original draft, writing – review & editing. Teng Wang: conceptualization, data curation, formal analysis, investigation, methodology, writing – original draft, writing – review & editing. Hui Ma: writing – review & editing. Kang Tang: writing – review & editing. Shuen Hou: writing – review & editing. Hongyun Jin: conceptualization, formal analysis, funding acquisition, investigation, project administration, resources, supervision,

validation, writing – review & editing. Guozhong Cao: writing – review & editing.

Conflicts of interest

There are no conflicts to declare.

Acknowledgements

This work was supported by the National Natural Science Foundation of China (51802292 and 21975230), Zhejiang Provincial Natural Science Foundation (LY20B010001), Major scientific and technological innovation in Hubei (2019AAA004 and 2018AAA015), Joint Fund of Ministry of Education (6141A02033239), and DONGFENG Project (91224Y180014).

References

1 Y. Gogotsi and R. M. Penner, *ACS Nano*, 2018, **12**, 2081–2083.
2 S. J. Luo, L. Y. Xie, F. Han, W. Wei, Y. Huang, H. Zhang, M. S. Zhu, O. G. Schmidt and L. Wang, *Adv. Funct. Mater.*, 2019, **29**, 1901136.
3 Y. Sun, S. Guo and H. Zhou, *Energy Environ. Sci.*, 2019, **12**, 825–840.
4 L. Kouchachvili, W. Yaïci and E. Entchev, *J. Power Sources*, 2018, **374**, 237–248.
5 M. Okubo, S. Ko, D. Dwibedi and A. Yamada, *J. Mater. Chem. A*, 2021, **9**, 7407–7421.
6 J. Vetter, P. Novák, M. R. Wagner, C. Veit, K. C. Möller, J. O. Besenhard, M. Winter, M. Wohlfahrt-Mehrens, C. Vogler and A. Hammouche, *J. Power Sources*, 2005, **147**, 269–281.
7 S. Chen, L. Qiu and H. M. Cheng, *Chem. Rev.*, 2020, **120**, 2811–2878.
8 P. Albertus, S. Babinec, S. Litzelman and A. Newman, *Nat. Energy*, 2017, **3**, 16–21.
9 B. D. Adams, J. Zheng, X. Ren, W. Xu and J.-G. Zhang, *Adv. Energy Mater.*, 2018, **8**, 1702097.
10 W.-J. Zhang, *J. Power Sources*, 2011, **196**, 13–24.
11 N. Hu, Z. Tang and P. K. Shen, *RSC Adv.*, 2018, **8**, 26589–26595.
12 V. G. Rocha, E. Saiz, I. S. Tirichenko and E. García-Tuñón, *J. Mater. Chem. A*, 2020, **8**, 15646–15657.
13 M. C. Wu, T. S. Zhao, H. R. Jiang, Y. K. Zeng and Y. X. Ren, *J. Power Sources*, 2017, **355**, 62–68.
14 S. Hariharan, V. Ramar, S. P. Joshi and P. Balaya, *RSC Adv.*, 2013, **3**, 6386.
15 P.-F. Wang, Y. You, Y.-X. Yin and Y.-G. Guo, *Adv. Energy Mater.*, 2018, **8**, 1701912.
16 Y. S. Yu, M. Farmand, C. Kim, Y. Liu, C. P. Grey, F. C. Strobridge, T. Tyliszczak, R. Celestre, P. Denes, J. Joseph, H. Krishnan, F. Maia, A. L. D. Kilcoyne, S. Marchesini, T. P. C. Leite, T. Warwick, H. Padmore, J. Cabana and D. A. Shapiro, *Nat. Commun.*, 2018, **9**, 921.
17 S. D. Lacey, D. J. Kirsch, Y. Li, J. T. Morgenstern, B. C. Zarket, Y. Yao, J. Dai, L. Q. Garcia, B. Liu, T. Gao, S. Xu, S. R. Raghavan, J. W. Connell, Y. Lin and L. Hu, *Adv. Mater.*, 2018, **30**, e1705651.
18 T. Wang, X. Tian, L. Li, L. Lu, S. Hou, G. Cao and H. Jin, *J. Mater. Chem. A*, 2020, **8**, 1749–1756.
19 K. Sun, T. S. Wei, B. Y. Ahn, J. Y. Seo, S. J. Dillon and J. A. Lewis, *Adv. Mater.*, 2013, **25**, 4539–4543.
20 L. J. Tan, W. Zhu and K. Zhou, *Adv. Funct. Mater.*, 2020, **30**, 2003062.
21 C. Han, Q. Fang, Y. Shi, S. B. Tor, C. K. Chua and K. Zhou, *Adv. Mater.*, 2020, **32**, e1903855.
22 J. W. Boley, K. Chaudhary, T. J. Ober, M. Khorasaninejad, W. T. Chen, E. Hanson, A. Kulkarni, J. Oh, J. Kim, L. K. Aagesen, A. Y. Zhu, F. Capasso, K. Thornton, P. V. Braun and J. A. Lewis, *Adv. Mater.*, 2017, **29**, 1604778.
23 C. Zhu, T. Liu, F. Qian, T. Y. Han, E. B. Duoss, J. D. Kuntz, C. M. Spadaccini, M. A. Worsley and Y. Li, *Nano Lett.*, 2016, **16**, 3448–3456.
24 M. Wei, F. Zhang, W. Wang, P. Alexandridis, C. Zhou and G. Wu, *J. Power Sources*, 2017, **354**, 134–147.
25 R. R. Kohlmeyer, A. J. Blake, J. O. Hardin, E. A. Carmona, J. Carpena-Núñez, B. Maruyama, J. Daniel Berrigan, H. Huang and M. F. Durstock, *J. Mater. Chem. A*, 2016, **4**, 16856–16864.
26 M. Cheng, Y. Jiang, W. Yao, Y. Yuan, R. Deivanayagam, T. Foroozan, Z. Huang, B. Song, R. Rojaee, T. Shokuhfar, Y. Pan, J. Lu and R. Shahbazian-Yassar, *Adv. Mater.*, 2018, **30**, e1800615.
27 J. Hu, Y. Jiang, S. Cui, Y. Duan, T. Liu, H. Guo, L. Lin, Y. Lin, J. Zheng, K. Amine and F. Pan, *Adv. Energy Mater.*, 2016, **6**, 1600856.
28 B. Yao, S. Chandrasekaran, J. Zhang, W. Xiao, F. Qian, C. Zhu, E. B. Duoss, C. M. Spadaccini, M. A. Worsley and Y. Li, *Joule*, 2019, **3**, 459–470.
29 B. Chen, Y. Jiang, X. Tang, Y. Pan and S. Hu, *ACS Appl. Mater. Interfaces*, 2017, **9**, 28433–28440.
30 M. A. Skylar-Scott, S. Gunasekaran and J. A. Lewis, *Proc. Natl. Acad. Sci. U. S. A.*, 2016, **113**, 6137–6142.
31 C. M. Larson, J. J. Choi, P. A. Gallardo, S. W. Henderson, M. D. Niemack, G. Rajagopalan and R. F. Shepherd, *Adv. Eng. Mater.*, 2016, **18**, 39–45.
32 J. A. Lewis, *Adv. Funct. Mater.*, 2006, **16**, 2193–2204.
33 X. Tian and K. Zhou, *Nanoscale*, 2020, **12**, 7416–7432.
34 H. Long, W. Zeng, H. Wang, M. Qian, Y. Liang and Z. Wang, *Adv. Sci.*, 2018, **5**, 1700634.
35 C. Shen, T. Wang, X. Xu and X. Tian, *Electrochim. Acta*, 2020, **349**, 136331.
36 G. Hernandez-Sosa, S. Tekoglu, S. Stolz, R. Eckstein, C. Teusch, J. Trapp, U. Lemmer, M. Hamburger and N. Mechau, *Adv. Mater.*, 2014, **26**, 3235–3240.
37 P. Chang, H. Mei, S. Zhou, K. G. Dassios and L. Cheng, *J. Mater. Chem. A*, 2019, **7**, 4230–4258.
38 Y. Wang, C. Chen, H. Xie, T. Gao, Y. Yao, G. Pastel, X. Han, Y. Li, J. Zhao, K. K. Fu and L. Hu, *Adv. Funct. Mater.*, 2017, **27**, 1703140.
39 L. Qiu, Z. He and D. Li, *Adv. Mater.*, 2018, **30**, 1704850.
40 N. Zhu, W. Liu, M. Xue, Z. Xie, D. Zhao, M. Zhang, J. Chen and T. Cao, *Electrochim. Acta*, 2010, **55**, 5813–5818.
41 K. Leng, F. Zhang, L. Zhang, T. Zhang, Y. Wu, Y. Lu, Y. Huang and Y. Chen, *Nano Res.*, 2013, **6**, 581–592.

